Journal of Environmental Chemical Engineering 6 (2018) 5999–6011

Contents lists available at ScienceDirect

Journal of Environmental Chemical Engineering

journal homepage: www.elsevier.com/locate/jece

Synthesis of CeO_2/TiO_2 nanotubes and heterogeneous photocatalytic degradation of methylene blue

Le Thi Thanh Tuyen[a,c], Dao Anh Quang[b], Tran Thanh Tam Toan[a], Truong Quy Tung[b], Tran Thai Hoa[a], Tran Xuan Mau[a], Dinh Quang Khieu[a,*]

[a] University of Sciences, Hue University, Hue City, 530000, Viet Nam
[b] Hue Industrial College, Hue City, 530000, Viet Nam
[c] Le Quy Don Gifted High School, Danang City, 550000, Viet Nam

ARTICLE INFO

Keywords:
CeO_2/TiO_2 nanotubes
Photocatalytic activity
Visible light
Box–Behnken design

ABSTRACT

In this study, the preparation of CeO_2/ TiO_2 nanotubes (CeO_2/TiO_2–NTs) is demonstrated using the hydrothermal method. The conditions for the synthesis were optimised using the Box–Behnken design. The samples obtained were characterised by means of X-ray diffraction, high-resolution transmission electron microscopy, energy dispersive X-ray spectroscopy, transmission electron microscopy, scanning electron microscopy, X-ray photoelectron spectroscopy, ultraviolet-visible diffuse reflectance spectroscopy, nitrogen adsorption/desorption isotherms, and Raman spectroscopy. The photocatalytic behaviour under visible light and kinetics of the CeO_2/TiO_2–NTs catalyst *via* methylene blue degradation were addressed. The results showed that the introduction of CeO_2 into TiO_2–NTs enhanced the photocatalytic activity in the visible light region. CeO_2/TiO_2–NTs were stable and potential as a visible light photocatalyst for the organic substances degradation in aqueous solutions.

1. Introduction

TiO_2 is classified as a semiconductor, widely used in photochemical techniques to decompose numerous kinds of toxic organic contaminants because of its outstanding features. TiO_2 is a low-cost non-toxic compound with high chemical durability, high photochemical stability and biological inertness [1,2]. Several oxide nanostructures of TiO_2 have been explored, including nanoparticles (0D) [3], nanowires (1D) [4], nanorods (1D) [5], nanofibers [6], and nanosheets (2D) [7]. The uniform dispersion of nanoparticles can be achieved in a liquid medium *via* electrostatic and steric stabilization. However, when the nanoparticles are consolidated into solid materials, the aggregation between the nanoparticles becomes very strong because the van der Waals attraction is inversely proportional to the particle size [8]. When the aggregates are large and dense, only the primary particles near the surface region of the secondary particles contribute to the catalytic reaction and the inner part becomes inactive. Under this configuration, a high catalytic activity cannot be achieved. The 1D nanostructures such as nanowires, nanorods, and nanotubes with a less agglomerated configuration have been used to improve the catalytic activity [4,7]. When photocatalytic titania (TiO_2) absorbs ultraviolet radiation from a light source, an electron of the valence band of titanium dioxide becomes excited. The excess energy of the excited electron promotes the electron to the conduction band of titanium dioxide, therefore creating a negative-electron (e–) and positive-hole (h^+) pair. The positive hole will oxidize water molecules to form hydrogen gas and hydroxyl radicals. The negative electron will reduce oxygen molecules to form a superoxide anion. This cycle continues when the light is available. As a result, these free radicals will decompose the organic contaminants [9,10]. In comparison with nanoparticles, TiO_2 nanotubes (denoted as TiO_2-NTs) possess photocatalytic features. Depending on the method of synthesis utilised, their preeminent features are: massive surface (up to 478 m^2/g), great volume of capillary (up to 1.25 cm^3/g) [11,12], capacity of transferring electrons from long distances [13], capacity of ion exchange [14], and noticeable capacity of absorbing light as a result of the considerable ratio between the length and the diameter of the tubes [15]. The transfer of the charge carriers along the length of the titania nanotubes has been considered to prevent the fast recombination of photoexcited electrons and positive holes [16,17]. Such unique characteristics of TiO_2-NTs result in enhanced photocatalytic activities and render them excellent candidates for photocatalytic applications. As for preparation techniques, the hydrothermal process is considered as the most effective to synthesise TiO_2-NTs with their large-sized capillary and nanotube unique structure [11,18–21]. This is the simplest method,

* Corresponding author.
E-mail address: dqkhieu@hueuni.edu.vn (D.Q. Khieu).

https://doi.org/10.1016/j.jece.2018.09.022
Received 13 June 2018; Received in revised form 13 August 2018; Accepted 16 September 2018
Available online 19 September 2018

as it is easy to carry out without the requirement of moulds or bases. Furthermore, the output nanotubes have their homogeneity with a noticeable surface and porosity.

To improve the photocatalytic efficiency of TiO_2, besides morphological modification attempts, wide employment of binary oxides based on TiO_2 has yielded a number of marked results. Binary oxide systems such as TiO_2–Fe_2O_3 [22], TiO_2–SnO_2 [23], TiO_2–Cu_2O [24], TiO_2–CeO_2 [25], and TiO_2–WO_3 [26] have been found to exhibit a much higher photocatalytic activity under visible light illumination than pure TiO_2 by accelerating the charge separation on the TiO_2 surface and extending the energy range of photoexcitation. Being one of the rare-earth metal oxides, CeO_2 has attracted a considerable attention due to its special electron orbital structure, unique optical and Ce^{3+}/Ce^{4+} redox behaviour, high thermal stability and large oxygen-storage capability. Surface defects such as oxygen vacancies working as electron traps can impede $e–/h^+$ recombination, and the 4f electron configuration can enhance the electron transfer from the adsorbed dye to oxygen species. Therefore, introducing CeO_2 to TiO_2 nanostructures could favour the improved separation of the electron-hole pairs, thus enhancing the photocatalytic performance of CeO_2–TiO_2 catalysts [27–30].

In practice, the influence of different synthesis parameters on the performance of the obtained photocatalysts is crucial. However, most of the published results concerning the relationship between the photocatalytic capacity of CeO_2–TiO_2 catalysts and various related parameters followed the conventional method [2,31,32,33,34]. Such a method is carried out by monitoring the effect of one factor at a time on an experimental response while maintaining other factors at a fixed level. This technique, therefore, does not consider the interactive effects of the variables and requires considerable resources including time and expenses for a large number of variables [35], whereas the optimisation of the procedures of synthesis by using multivariate statistic techniques allows the simultaneous variation of many experimental factors. The multivariable optimisation has been considered to be faster, more economical and effective in identifying the best conditions and maximising desirable responses in any experimental subjects. However, to the best of our knowledge, there are only a few reports available in the literature regarding the optimization of the CeO_2–TiO_2 preparation conditions in the photocatalytic degradation [1,36].

In the present work, the effective variables of the preparation of CeO_2/TiO_2-NTs) for the photocatalytic degradation of methylene blue (MB) under visible light were optimised utilising the Box–Behnken design (BBD) of response surface methodology (RSM) for the maximal photocatalytic yield. The photocatalytic behaviour and kinetics studies of the photocatalytic degradation of methylene blue (MB) were investigated.

2. Experimental

2.1. Materials

Cerium (III) nitrate hexahydrate ($Ce(NO_3)_3.6H_2O$, Merck, Germany, 99%), titanium (IV) oxide, anatase (TiO_2, DaeJung, Korea, 98%), methylene blue (MB) ($C_{16}H_{18}ClN_3S$, Merck, Germany), P25 (TiO_2, Degussa, Germany, 99,5%); NaOH, $NH_3.H_2O$ (Sinofarm Chemical Reagent Co., Ltd., China, 25%–28%) and HCl (Sinofarm Chemical Reagent Co., Ltd., China) were used as received without further purification. Methylene blue ($C_{16}H_{18}ClN_3S$, Merck, 99%) was used as a dye model. The molecular formula is presented in Fig. 1.

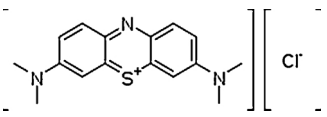

Fig. 1. Molecular formula of methylene blue (MB).

2.2. Preparation of CeO_2/TiO_2–NTs

TiO_2–NTs were synthesised by using a hydrothermal route, which has been reported in detail in some literature [17,37–39] (see Fig. 2). In brief, 3 g of TiO_2 powder was dispersed in 70 mL of a 10 M NaOH solution and the mixture was then sonicated continuously for 30 min. Afterwards, the suspension was transferred to a 100 mL Teflon-lined autoclave and hydrothermally treated at temperatures 140, 160, and 180 °C for a specific time (18, 20 and 22 h). The suspension was then filtered, and the powder was washed several times with distilled water and 0.1 M HCl until the pH of the leaching water reached 7, followed by air-drying at 100 °C. Thus, TiO_2–NTs were obtained. The CeO_2/TiO_2–NTs catalyst was prepared with the impregnation method described by Zhao et al. [40] as follows: 0.8 g of the as-prepared TiO_2–NTs was dispersed in a specific amount of the aqueous solution of 0.02 M Ce $(NO_3)_3$ under magnetic stirring for 2 h at room temperature. Simultaneously, a sufficient amount of $NH_3.H_2O$ solution was added drop-wise into the suspension under vigorous stirring to reach pH about 10. After being aged for 4 h at room temperature, the obtained product was dried at 100 °C for 12 h. The resultant CeO_2/TiO_2–NTs were finally calcined at a certain temperature for a specific time according to the Box-Behnken design and designated as CeO_2/TiO_2–NTs (Fig. 2).

According to initial experiments, four factors, namely hydrothermal temperature (X_1), calcination temperature (X_2), hydrothermal time (X_3), and CeO_2/TiO_2 ratio (mol/mol) (X_4) were considered to affect the catalytic properties of CeO_2/TiO_2–NTs in the degradation of methylene blue. In the present study, the experimental design of Box–Behnken [41–45] was employed to determine the optimum levels of the variables. The number of experiments (N) required for this design is $N = 2{\cdot}k{\cdot}(k–1) + C_0$, where k is the factor number and C_0 is the replicate number of the central point [44]. Thus, a total of 27 runs were performed for optimizing these four variables in the current Box–Behnken design with 3 runs at the central point. The response of this design was the yield of the degradation reaction (Y). The corresponding symbols and levels are shown in Table 1.

Based on the experimental data, a second-order polynomial model was calculated, which provided the relationship between the photocatalytic degradation yield and the four selected variables. The relationship was represented as follows:

$$Y = \beta_0 + \sum_{i=1}^{4} \beta_i{\cdot}X_i + \sum_{i=1}^{4} \beta_{ii}{\cdot}X_i^2 + \sum_{i=1}^{3}\sum_{j>i}^{4} \beta_{ij}{\cdot}X_i{\cdot}X_j \quad (1)$$

where Y (%) is the predicted response value; β_0 is the intercept term, β_i is the linear coefficients; β_{ij} is the cross-product coefficients, β_{ii} is the quadratic term coefficients, and X_i, X_j are the independent variables.

The design and analysis of this experiment were carried out using statistical software MINITAB version 16.

2.3. Photocatalytic degradation experiments

The photocatalytic activity of the synthesised CeO_2/TiO_2–NTs was evaluated by studying the degradation of MB in water (100 mL, 15 mg/L, neutral pH) under the filtrated light of a 250 W fluorescent high-pressure mercury lamp (Philip ML 250 W) as a visible light source. The distance maintained between the lamp and the solution surface was 15 cm in all measurements (Fig. 3).

The experiments were conducted under magnetically stirring for 30 min in the dark, at room temperature to reach the adsorption-desorption equilibrium; then, the mixture was illuminated with periodic sampling (5 mL, 20 min). The samples taken from the mixture were immediately centrifuged and the filtrates were then analysed by recording the absorbance at 664 nm with a UV–vis spectrophotometer (UViline 9400).

The degradation efficiency of MB was calculated according to expression (2)

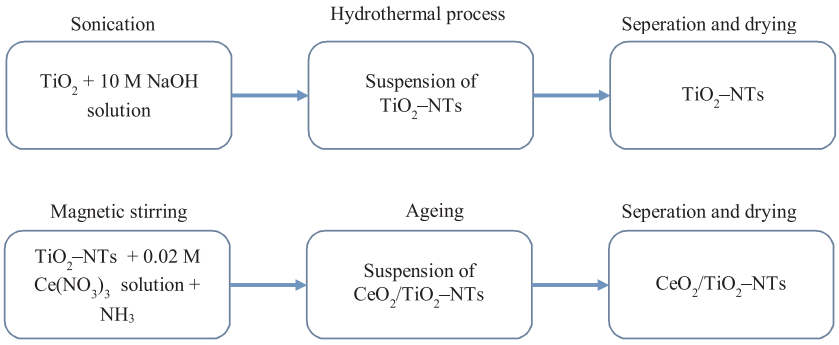

Fig. 2. Flow chart of the preparation of CeO_2/TiO_2–NTs.

Table 1
Factors and their levels in the full factorial design.

Factors	Low	Medium	High
Hydrothermal temperature, °C (X_1)	140	160	180
Calcination temperature, °C (X_2)	500	550	600
Hydrothermal time, h (X_3)	18	20	22
CeO_2/TiO_2 ratio, mol/mol (X_4)	0.1	0.3	0.5
Coded levels	–1	0	1

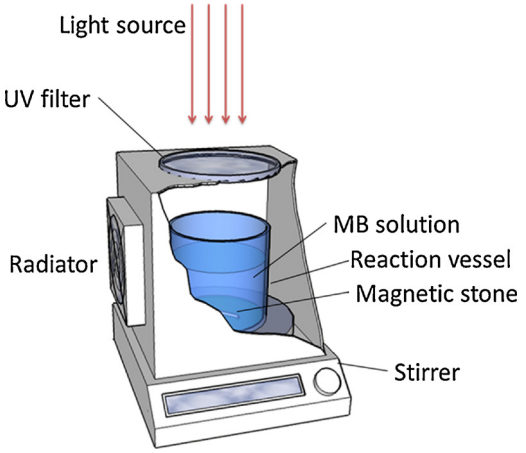

Fig. 3. Equipment for the photocatalytic experiment.

$$F = \frac{C_0 - C}{C_0} \cdot 100\,\% \quad (2)$$

where C_0 and C are the concentration of the initial and remaining MB, respectively.

The analysis of $OH^{\cdot}$ formation on the sample surface under light illumination was conducted by means of fluorescence spectroscopy using terephthalic acid, which readily reacted with $OH^{\cdot}$ to produce a highly fluorescent product, 2-hydroxyterephthalic acid [46,47]. Briefly, 200 mg of the obtained CeO_2/TiO_2–NTs was added to 200 mL of a $5{\cdot}10^{-4}$ M terephthalic acid solution in $2{\cdot}10^{-3}$ M NaOH, and then the light illumination of the solution started. Sampling was carried out every 20 min. The solution after filtration was analysed on a fluorescence spectrophotometer. The product of terephthalic acid hydroxylation – 2-hydroxyterephthalic acid – gave a peak at the wavelength of about 425 nm by the excitation with the wavelength of 315 nm.

The chemical oxygen demand (COD) of MB solution was measured using the ASTM method [48]. The sample was oxidised by a boiling mixture of chromic and sulfuric acids and refluxed in a strong acid solution with a known excess of potassium dichromate ($K_2Cr_2O_7$). After digestion, the remaining unreduced $K_2Cr_2O_7$ was titrated with ferrous ammonium sulfate to determine the amount of $K_2Cr_2O_7$ consumed, and the oxidisable matter was calculated in terms of oxygen equivalent. The samples were analysed in replicates to yield the most reliable data.

2.4. Characterisation techniques

The X-ray powder diffraction (XRD) patterns were collected with a D8 Advance Bruker X-ray diffractometer using CuK_α radiation (1.54 Å). The Raman spectra were measured at room temperature using a Horiba Xplora Raman spectrophotometer with the excitation laser wavelength of 532 nm. The transmission electron microscopy (TEM) and scanning electron microscopy (SEM) images were collected using a JEOL JEM – 2100 F (USA) transmission electron microscope and an SEM JMS–5300LV (USA) scanning electron microscope, respectively. The elemental composition was determined by means of electron dispersive X-ray (EDX) analysis coupled with HRTEM using JEOL 2100, EDX detector with XMax 80 T (Oxford). The atomic absorption measurements (AAS) were made using a Shimadzu AA–7000 flame atomic absorption spectrometer (Japan). The X-ray photoelectron spectroscopy (XPS) analysis was carried out using a Shimadzu Kratos Axisultra DLD spectrometer with AlKα as the excitation source. The calibration of the binding energy and the corrections of the energy shift were accomplished by assuming that the C_{1s} line lies at 284.6 eV. The diffuse reflectance spectra (DRS) were measured using a Cary5000 UV–Vis–NIR spectrophotometer, and reflectance spectra were referenced to $BaSO_4$. The nitrogen adsorption-desorption isotherms were performed using a Micromeritics Tristar 3000 device (USA). The Shimadzu RF–5301 PC series fluorescence spectrometer was used to collect the fluorescence emission spectra of the samples.

The point of zero charge (pH_{PZC}) of CeO_2/TiO_2–NTs was estimated using the pH drift method [49,50]. Five millilitres of 0.1 M NaCl solution and 40 mL of distilled water were added to a series of 100 mL flasks. The initial pH value (pH_i) of the solution was adjusted from 2 to 12 by using either 0.1 M NaOH or 0.1 M HCl solutions. The total volume of solution in each flask was made exactly to 50 mL by adding distilled water. The 0.01 M NaCl solutions with different pH value were obtained. Then, 0.1 g of CeO_2/TiO_2–NTs was added to each flask, and the mixtures were stirred for 24 h; the final pH (pH_f) of the solutions was measured. The difference between the initial pH and final pH ($\Delta pH = pH_i - pH_f$) was plotted against pH_i. The point of intersection of the curve with the abscissa, at which $\Delta pH = 0$, provided pH_{PZC}.

3. Results and discussion

3.1. Preparation of CeO_2/TiO_2–NTs using Box–Behnken design

The experimental design matrix of Box–Behnken (B–B) and the results derived from each experiment are represented in Table 2.

According to the polynomial regression model, the correlation of photocatalytic degradation yield to corresponding coded values (x_1, x_2, x_3, and x_4) of the four variables (hydrothermal temperature, calcination temperature, hydrothermal time and CeO_2/TiO_2 ratio, respectively) was obtained as

Table 2
Experimental design in coded units and response.

Exp.	x_1	x_2	x_3	x_4	Yield / %
1	0	−1	0	1	0.722
2	−1	0	1	0	0.670
3	0	0	−1	1	0.768
4	1	0	1	0	0.721
5	0	−1	0	−1	0.819
6	−1	0	0	1	0.723
7	0	0	0	0	0.874
8	0	1	0	1	0.772
9	0	1	0	−1	0.870
10	1	0	0	−1	0.872
11	−1	0	−1	0	0.720
12	1	1	0	0	0.768
13	0	0	1	−1	0.821
14	0	1	1	0	0.719
15	1	0	−1	0	0.773
16	0	0	0	0	0.874
17	0	0	0	0	0.873
18	0	1	−1	0	0.769
19	−1	0	0	−1	0.822
20	0	−1	1	0	0.670
21	0	−1	−1	0	0.718
22	−1	1	0	0	0.721
23	0	0	1	1	0.719
24	1	−1	0	0	0.723
25	0	0	−1	−1	0.872
26	−1	−1	0	0	0.672
27	1	0	0	1	0.770

$$Y = 0.8740 + 0.0249{\cdot}x_1 + 0.0246{\cdot}x_2 - 0.0250{\cdot}x_3 - 0.0502{\cdot}x_4 - 0.0755{\cdot}x_1^2 - 0.0770{\cdot}x_2^2 - 0.0774{\cdot}x_3^2 - 0.0012{\cdot}x_4^2 - 0.0010{\cdot}x_1{\cdot}x_2 - 0.0005{\cdot}x_1{\cdot}x_3 - 0.0008{\cdot}x_1{\cdot}x_4 - 0.0005{\cdot}x_2{\cdot}x_3 - 0.0003{\cdot}x_2{\cdot}x_4 + 0.0005{\cdot}x_3{\cdot}x_4 \quad (3)$$

The analysis of variance proved the goodness-of-fit of the models (Table 3). The determination coefficient R^2 for the degradation yield was calculated as 99.97%, suggesting a good performance for the developed model. R^2 adjusted to the degradation yield was 99.94%, *i.e.*, the developed model for the prediction of the extraction yield marginally differs by ± 0.06% from the experimental data. The adequacy test is significant at p-values < 0.05, confirming the adequacy of the selected quadratic model. According to the statistical results with the 95% confidence level, each term in the model is significant when its p-value is less than 0.05 (Table 4). Therefore, the reduced form of the regression equation was expressed as follows:

$$Y = 0.8740 + 0.0249{\cdot}x_1 + 0.0246{\cdot}x_2 - 0.0250{\cdot}x_3 - 0.0502{\cdot}x_4 - 0.0755{\cdot}x_1^2 - 0.0770{\cdot}x_2^2 - 0.0774{\cdot}x_3^2 \quad (4)$$

In the regression equation, a negative sign suggested an antagonistic effect, whereas a positive sign indicated a synergistic effect. From Eq. (4), the similar positive value of the parameter estimate for variables x_1 and x_2 indicated the same level of significance whereas x_3 and x_4 showed the negative relationship.

In this study, the response optimisation by desirability function of the response surface methodology was employed to find out the optimal parameters to seek for the maximal photocatalytic degradation yield.

Table 3
ANOVA for the fit of the experimental data to the response surface.

Source	Degree of freedom	Adjusted sum of squares	Adjusted mean squares	p-value
Regression	14	0.122255	0.008732	0.000
Linear	4	0.052403	0.013101	0.000
Square	4	0.069843	0.017461	0.000
Interaction	6	0.000009	0.000002	0.746
Residual error	12	0.000033	0.000003	
Lack-of-fit	10	0.000033	0.000003	0.096
Pure error	2	0.000001	0.000000	
Total	26	0.122288		

Table 4
ANOVA for the degradation yield.

Source	Regression coefficient	F-value	p-value
x_1	0.0249	2688.75	0.00
x_2	0.0246	2617.29	0.00
x_3	–0.0250	2706.77	0.00
x_4	–0.0502	10899.37	0.00
x_1^2	–0.0755	10984.02	0.00
x_2^2	–0.0770	11424.56	0.00
x_3^2	–0.0774	11536.05	0.00
x_4^2	–0.0012	2.62	0.13
$x_1{\cdot}x_2$	–0.0010	1.44	0.25
$x_1{\cdot}x_3$	–0.0005	0.36	0.56
$x_1{\cdot}x_4$	–0.0008	0.81	0.39
$x_2{\cdot}x_3$	–0.0005	0.36	0.56
$x_2{\cdot}x_4$	–0.0003	0.09	0.77
$x_3{\cdot}x_4$	0.0005	0.36	0.56
Model		7.22	0.001

The profile for predicted values in MINITAB 16 was employed for the optimisation process. The optimisation design matrix (Fig. 4) represents the maximal photocatalytic degradation (92.9% for MB) at the conditions set: hydrothermal temperature (163 °C), calcination temperature (557 °C), hydrothermal time (20 h), and CeO_2/TiO_2 ratio (0.1 mol·mol^{-1}). The reliability of this prediction was examined by the performance of five similar experiments at the optimal conditions. The experimental degradation yield was 93%, 96%, 94.5%, 95% and 94.2%. The one-sample t-test showed a non-significant difference with respective values presented by the model (t (4) = –2.32, p = 0.08). Therefore, the optimal synthesis conditions were used to synthesise the CeO_2/TiO_2–NTs for further experiments.

3.2. Characterisation of catalysts

The XRD patterns of the as-synthesized TiO_2–NTs, TiO_2–NTs 550 (TiO_2–NTs calcinated at 550 °C) and CeO_2/TiO_2–NTs (prepared at optimal conditions) are shown in Fig. 5. It can be seen clearly that the as-synthesized TiO_2–NTs mainly consist of amorphous phases with low diffraction intensity, showing poor crystallinity. However, after being calcinated at 550 °C, the characteristic diffractions indexed as anatase phase (JCPDS: 00-021-1272) were observed. In addition, the diffraction peak around 43°, which can be assigned to the rutile (210) (JCPDS: 00-021-1276) was detected, revealing the remaining of the rutile phase in TiO_2–NTs.

The presence of CeO_2 in the CeO_2/TiO_2–NTs sample is based on the appearance of (101) and (200) characteristic peaks (JCPDS: 00-034-0394). The existence of the mixture of anatase and rutile with ceria indicated the formation of CeO_2–TiO_2 composite. As shown in Fig. 6a and b, the aggregated CeO_2 nanoparticles ranging from 5 to 10 nm in size on the surface of the TiO_2 nanotubes could be clearly observed. The TiO_2 nanotubes were hollow and open-ended with an average inner diameter of 4 nm, an average outer diameter of 10 nm, and about 200 nm in length. Ceria dispersed mainly on the surface of TiO_2 nanotubes and, therefore, formed a boundary between those particles and the TiO_2 nanotubes. This was confirmed by the measured lattice spacing d of 0.27 nm due to (200) planes of CeO_2 and d of 0.35 nm due to (101) of TiO_2 obtained from the high-resolution HR–TEM image (Fig. 6c). Furthermore, the EDX spectra of the sample CeO_2/TiO_2–NTs in Fig. 6d confirmed the presence of titanium, cerium and oxygen in the sample of CeO_2/TiO_2-NTs.

The textural properties of the resulting materials were investigated by means of nitrogen adsorption/desorption isotherms (Fig. 7). The curves of the N_2 adsorption-desorption isotherms for all samples were similar, in which TiO_2–NTs, TiO_2–NTs 550, and CeO_2/TiO_2–NTs

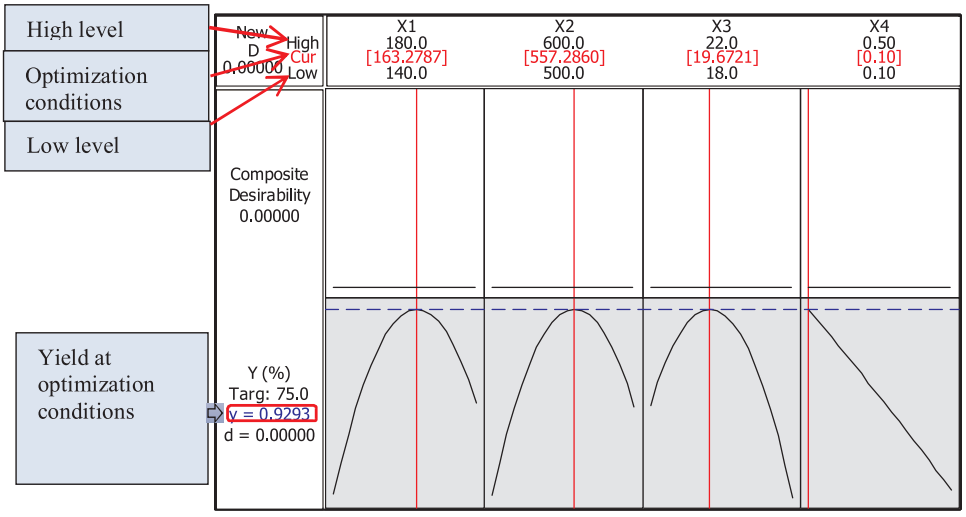

Fig. 4. Optimisation plots for the photocatalytic degradation yield of MB over CeO_2/TiO_2–NTs.

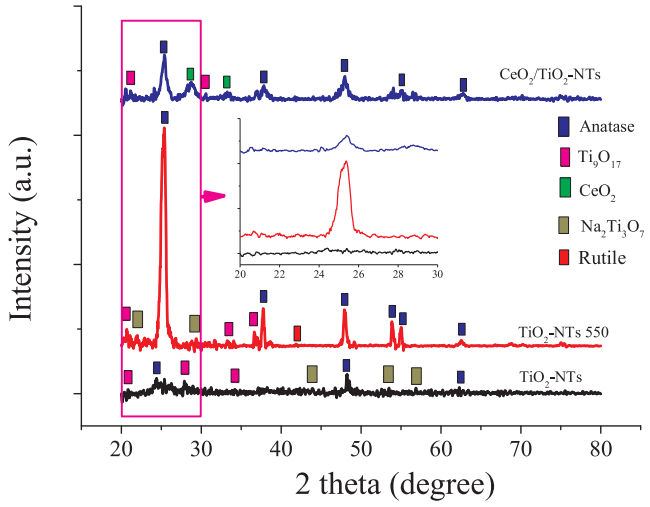

Fig. 5. XRD patterns of TiO_2–NTs; TiO_2–NTs 550; CeO_2/TiO_2–NTs.

exhibited the type IV isotherm according to IUPAC classification, indicating the mesoporous structure of the materials, and the type H3 hysteresis loop suggesting the presence of slit-shaped pores. The synthesised TiO_2–NTs had a much higher BET surface area (247 $m^2 g^{-1}$) than both TiO_2–NTs 550 (64 $m^2 g^{-1}$) and CeO_2/TiO_2–NTs (66 $m^2 g^{-1}$).

The XPS spectra were used to determine the elemental chemical state on the surface of the synthesised CeO_2/TiO_2–NTs, and the XPS analysis of Ce 3d, Ti 2d and O 1 s is demonstrated in Fig. 8. The Ce 3d spectrum (Fig. 8a) was relatively complex, and the identification of the chemical states of Ce 3d was labelled according to the convention established by Burroughs et al. [51], where *v* and *u* indicate the spin-orbit coupling states of $3d_{5/2}$ and $3d_{3/2}$, respectively. The binding energy of Ce $3d_{5/2}$ at 881, 885.5, 887.8, and 897.6 eV corresponded with v_0, v', v'' and v''', while the binding energy of Ce $3d_{3/2}$ at 899.4, 902, 907.2 and 916.1 eV was respective for u_0, u', u'' and u'''. The peaks at v_0, v', u_0 and u' were characteristic of Ce^{3+}, where u'/v' was related to the Ce ($3d^9 4f^1$) O ($2p^6$) final state, and u_0/v_0 was assigned to the Ce ($3d^9 4f^2$) O ($2p^5$) state [52,53]. The peaks labelled as v'', v''', u'', and u''' were attributed to Ce^{4+} in CeO_2 [40,52,54]. u'''/v''' was ascribed to the primary photoemission from Ce^{4+}–O_2 [55], corresponding with the Ce ($3d^9 4f^0$) O ($2p^6$) state. The u''/v'' doublet was resulting from the transfer of two electrons from the O 2p orbital to an empty Ce 4f orbital with the ($3d^9 4f^1$) O ($2p^5$) final state. The transfer of electrons from the O 2p to Ce 4f orbitals in the photoemission would increase the electron density of Ce^{4+}, thus decreasing the attraction of the Ce nucleus towards the electrons on the outermost layer while enhancing the repulsion between electrons. This is also why the more electrons were transferred from the O 2p orbitals, the poorer the binding energy of the Ce^{4+} 3d core level would become [56]. Based on these observations, it can be concluded that a mixture of Ce^{4+}/Ce^{3+} oxidation states existed on the surface of the synthesised CeO_2/TiO_2–NTs catalyst. The results were well in line with previous photoemission data reported by several authors on CeO_2/TiO_2 nanotube materials [2,40,57,36,58], as well as mixed CeO_2/TiO_2 materials obtained *via* other synthesis methods with different morphologies [25,53,56,59,60]. Concretely, Graciani et al. have used density functional calculations to demonstrate that Ce^{3+} ions are strongly stabilised due to the energy decrease of the Ce 4f levels as a result of mixing with the O 2p band of titania at the ceria-titania interface [61]. It is clear that the vehement interaction between CeO_2 and TiO_2 promoted the reduction of Ce^{4+} to Ce^{3+} and led to the presence of Ce^{3+} in the CeO_2/TiO_2 materials. Fig. 8b shows the Ti 2p core-level spectrum of CeO_2/TiO_2–NTs. The binding energies of Ti $2p_{3/2}$ and $2p_{1/2}$ in CeO_2/TiO_2–NTs were 458.4 and 464.2 eV, corresponding with typical characteristics of the octahedral coordinated Ti^{4+} ions [62]. The presence of CeO_2 maintained the binding energies of Ti 2p, and Ti existed as Ti^{4+} in the doped materials, which is in accordance with the previously reported results [25,56]. The O 1 s spectra (Fig. 8c) emerged widely and unsymmetrically, which indicates that at least three types of oxygen constituents were present at the material surface. The two peaks located at 528.8 and 530.0 eV could be ascribed to the O 1 s electron binding energy of oxygen (O^{2-}) in anatase TiO_2 and/or CeO_2. And the fitting data at 532.2 eV should be assigned to the hydroxyl groups in the material [63–65].

The Raman spectra were employed to define the lattice structure of the CeO_2–TiO_2 composite (Fig. 9). The result outputs asserted the existence of anatase in both samples synthesised, *via* the presence of characteristic signals for the tetragonal phase of anatase around 142 cm^{-1}; 395 cm^{-1}, 515 cm^{-1} and 637 cm^{-1} [66–71]. The shoulder at 195 cm^{-1} was also contributed to anatase [72]. The CeO_2 /TiO_2–NTs sample provided a strong band centred at 464 cm^{-1}, which was attributed to the typical vibrational mode of the cubic fluorite lattice [54,60,73]. The observed band at 241 $cm^{-1}$was assigned to the surface mode of the CeO_2(111) surface, and in a good agreement with the Raman spectra of ceria (CeO_2) powders with varying crystal sizes [74]. In addition, an increased peak at 195 cm^{-1} was attributed to the lattice mode (Na–O–Ti peaks) according to Marques et al. [75]. This result again confirms that CeO_2 was associated with titania on the anatase structure.

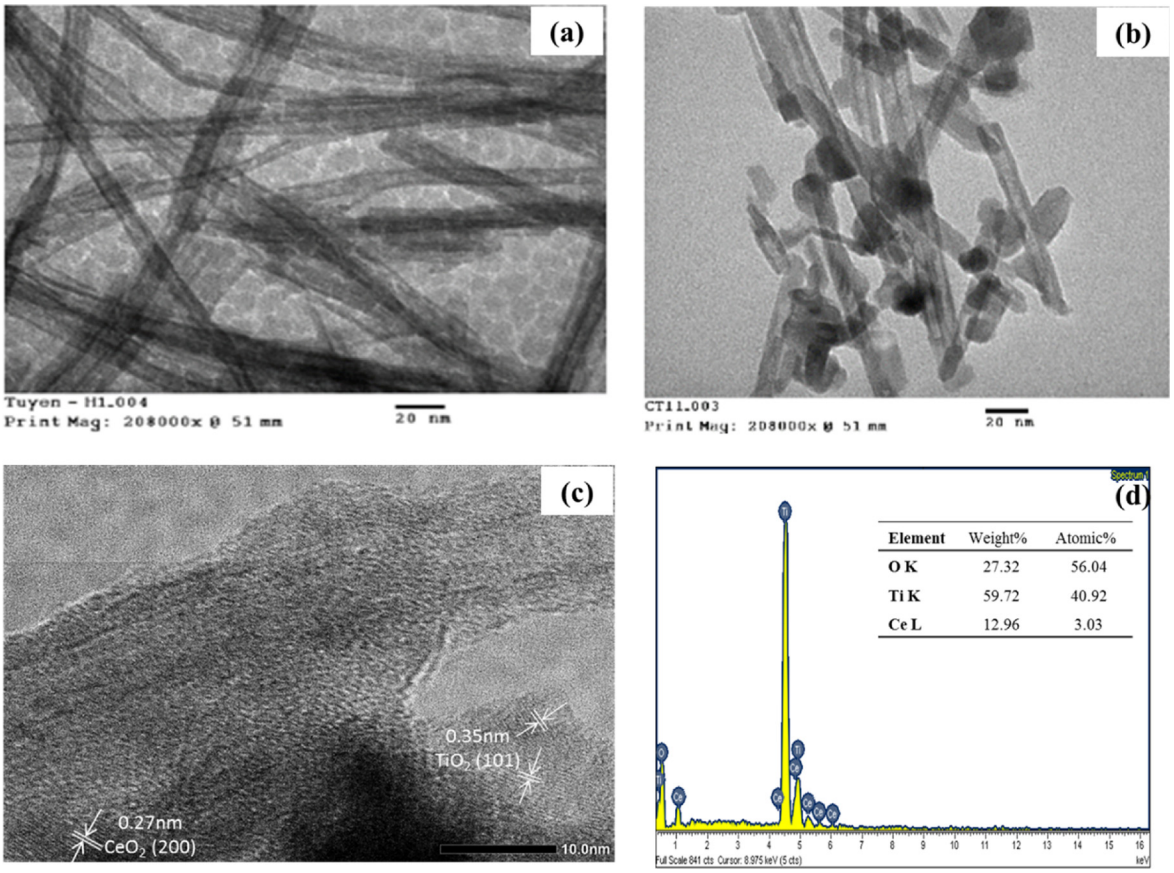

Fig. 6. TEM images of (a) TiO_2–NTs, (b) CeO_2/TiO_2–NTs, (c) HRTEM image of CeO_2/TiO_2–NTs and (d) EDX spectrum of CeO_2/TiO_2–NTs.

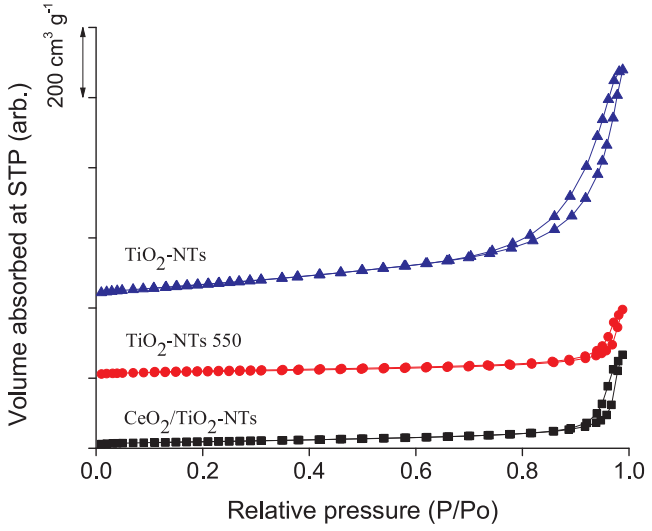

Fig. 7. Nitrogen adsorption/desorption isotherms of TiO_2–NTs, TiO_2–NTs 550, and CeO_2/TiO_2–NTs.

In order to investigate the electronic states of the catalysts, the UV–vis diffuse reflectance spectroscopy (DRS) studies were performed on TiO_2–NTs 550, CeO_2 and CeO_2/TiO_2–NTs. Compared with bare TiO_2-TiO_2 and bare CeO_2, CeO_2/TiO_2–NTs clearly exhibited broader absorption in the visible region (λ = 400–600 nm), displaying a slight red shift in the optical adsorption (Fig. 10a). The band gap (E_g) of the as-prepared samples could also be calculated by using Tauc's expression: $\alpha \cdot h \cdot \upsilon = A \cdot (h \cdot \upsilon - E_g)^{\frac{1}{2}}$, (where α is the absorption coefficient, A is the parameter that is related to the effective mass associated with the valence and conduction bands; h is the Planck constant; υ is the frequency [76]. The band gap values were calculated by plotting $(\alpha \cdot h \cdot \upsilon)^{\frac{1}{2}}$ *versus* $h \cdot \upsilon$. The band gap of CeO_2/TiO_2–NTs was found to be 2.64 eV, lower than that of TiO_2–NTs (3.08 eV) and CeO_2 (2.93 eV) (Fig. 10b). This red shift of the adsorption edge indicated the enhanced ability of the CeO_2/TiO_2–NTs hybrid catalyst to absorb visible light. The red shift in the optical transition, as well as the decreased band gap value of the CeO_2/TiO_2–NTs composite, was suggested to be relative to the presence of the Ce^{3+} ions with one electron in the strong localised 4f orbitals as observed from the XPS spectra. The existence of the Ce^{3+} ions in the synthesised CeO_2/TiO_2–NTs with respect to the 4f occupation ($4f^1$) resulted in an additional energy state, leading to the visible light absorption *via* the electron transfer transition from 4f to 5d orbitals, and thus reducing the band gap [56,65,77].

The band edge energy at the interface of the *n*-semiconductor was calculated according to the equations proposed by Xu and Schoonen as follows [78]:

$$E_{CB} = \chi - E_e - 0.5 \cdot E_g \quad (5)$$

$$E_{VB} = E_g - E_{CB} \quad (6)$$

where E_{CB} is the conduction band edge energy; E_{VB} is the valence band edge energy; χ is the electronegativity (χ = 5.56 eV for CeO_2 and χ = 5.81 eV for TiO_2 [79]); E_e is the free energy of electrons with respect to the normal hydrogen electrode (NHE) (E_e = 4,5 eV [79]); E_g is the band gap of the semiconductor.

The values of E_{CB} and E_{VB} for TiO_2 calculated from Eqs. (5) and (6) were –0.23 and 2.85 eV, respectively; and those for CeO_2 were –0.405 and 2.525 eV, respectively. The position of energy levels of CeO_2 and TiO_2 is illustrated in Fig. 11. It can be seen from the figure that the promoted photocatalytic activity of CeO_2/TiO_2-NTs is expected for two reasons: (i) the strong light adsorption of CeO_2 in the visible region, (ii)

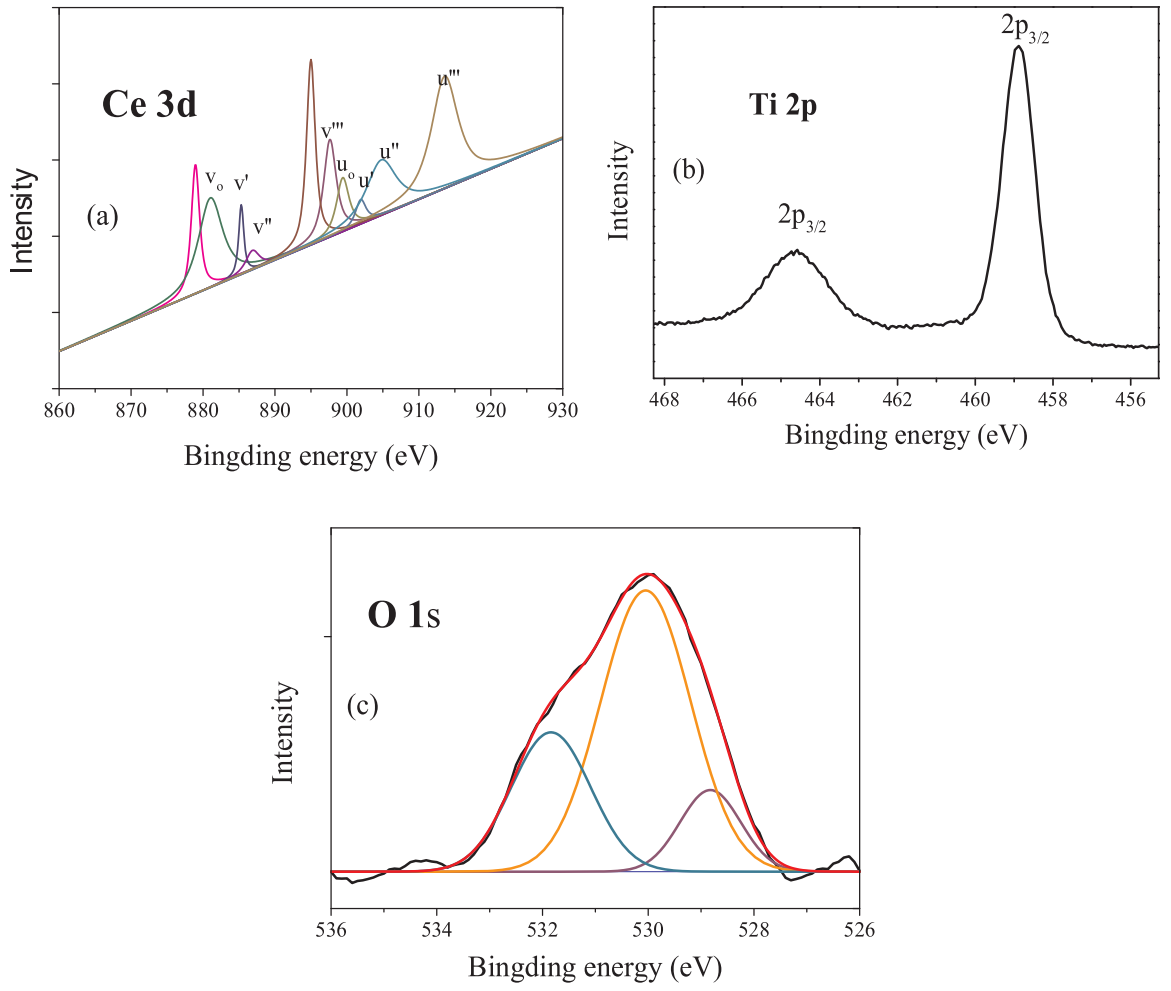

Fig. 8. XPS spectra of a) Ce 3d; b)Ti 2p, and c)O 1 s for CeO_2/TiO_2–NTs.

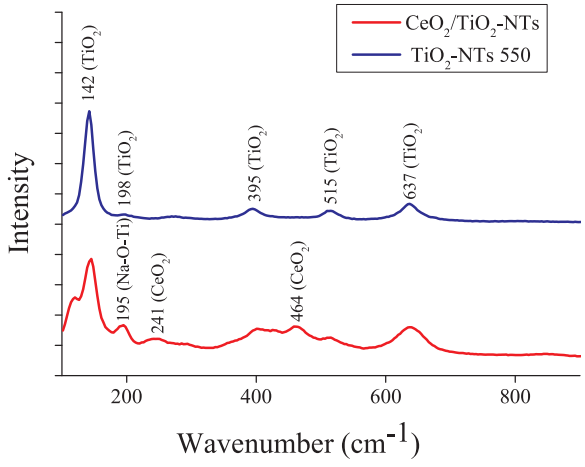

Fig. 9. Raman spectra of TiO_2–NTs 550 and CeO_2/TiO_2–NTs.

the transfer of electrons from E_{CB} of CeO_2 to E_{CB} of TiO_2 has been considered to prevent the fast recombination of photoexcited e^- and h^+.

3.3. Photocatalytic activity

3.3.1. Photocatalytic behaviours of CeO_2/TiO_2–NTs

3.3.1.1. Comparison of several catalysts. The adsorption kinetics and photocatalytic kinetics over several catalysts (TiO_2–NTs 550, CeO_2, CeO_2/TiO_2–NTs, and commercial P25 for the sake of comparison) are represented in Fig. 12. The degradation efficiency of MB was close to zero after light illumination for 150 min without a catalyst (blank sample). This means that the photolysis of MB was negligible. The MB adsorption over CeO_2 and TiO_2-NTs was around 5% and 90% under dark adsorption. Subsequently, the degradation efficiency of MB remained constant around these values when visible light was applied for a further 120 min, indicating that CeO_2 or TiO_2-NTs could not catalyse the photodegradation of MB under these conditions. Meanwhile, CeO_2/TiO_2–NTs and P25 exhibited a different behaviour towards the MB solution. After dark adsorption when the discolouring of MB was 68% for the former and 15% for the latter, these two materials exhibited catalytic activity under light illumination. CeO_2/TiO_2–NTs provided a photodegradation efficiency of MB at 94.6% after 60 min of irradiation and practically 100% after 120 min, while P25 produced a degradation efficiency of only 68% after 120 min of illumination. These results indicated that the composite of TiO_2 and CeO_2 successfully improved the photodegradation capability of TiO_2 nanotubes.

The UV–Vis spectra for the photocatalytic degradation of MB over CeO_2/TiO_2–NTs showed that the maximum absorption at 664 nm (electron transfer π–π* in the MB structure) decreased with the increase in light illumination time (Fig. 13a). To confirm the mineralisation of MB over CeO_2/TiO_2–NTs catalyst, the change of COD of reaction products with time was analysed (Fig. 13b). The initial COD was 28.2 mg L^{-1}, and its decrease became faster as the illumination time increased, reaching 10.68 mg L^{-1} after 120 min. These results confirmed the effectiveness of CeO_2/TiO_2–NTs as a photocatalyst for MB degradation under visible light. After 120 min of illumination, the total

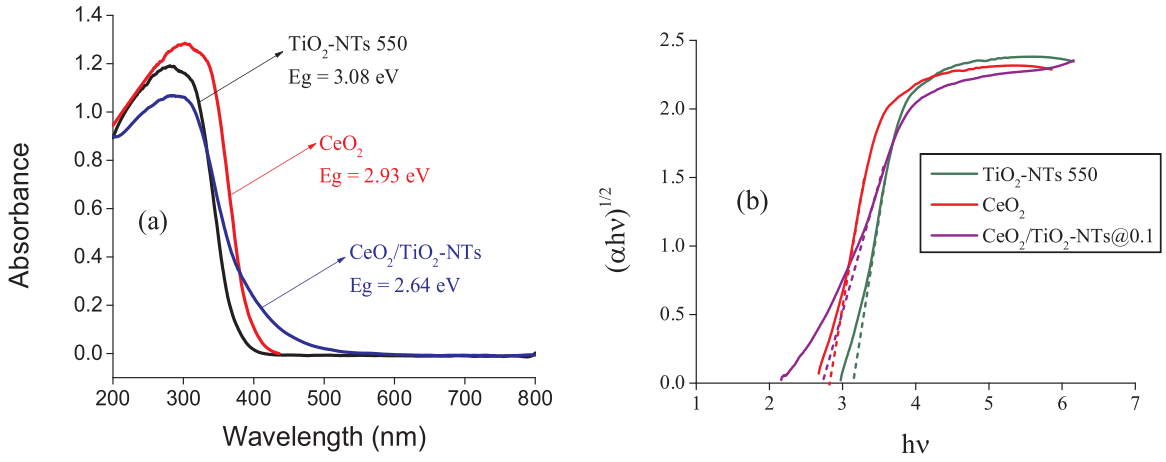

Fig. 10. a) UV–Vis diffuse reflectance spectra and b) Tauc' plots of TiO_2–NTs, CeO_2, and CeO_2/TiO_2–NTs.

decolourisation of MB practically occurred, while around 37.9% of COD reduction was obtained. The difference between the degradation and mineralisation could be attributed to the existence of intermediate products.

3.3.1.2. Leaching experiment. The contribution of the active metal ions leached from the solid catalyst in the total catalytic activity is an important problem in the application of heterogeneous catalysts for liquid phase processes [80]. The leaching experiment was carried out in the way that CeO_2/TiO_2–NTs catalyst was filtered after 70 min of reaction (Fig. 14). The MB conversion stopped at an 85% efficiency despite the fact that light continued to illuminate a further 80 min, and Ti and Ce were also absent in the solution (AAS analysis). This indicates that the catalyst was stable under working conditions. CeO_2/TiO_2–NTs was a true heterogeneous catalyst in the MB photocatalytic degradation.

3.3.1.3. Effect of pH. pH of the solution is one of the important factors affecting the efficiency of decomposition of organic matter during photochemical catalysis [81]. This decomposition is significantly dependent on the number of the adsorbed dye cations and the OH radicals on the surface of the catalyst, and this, in turn, depends on the state of the catalyst surface.

The MB degradation efficiency increased sharply when pH increased

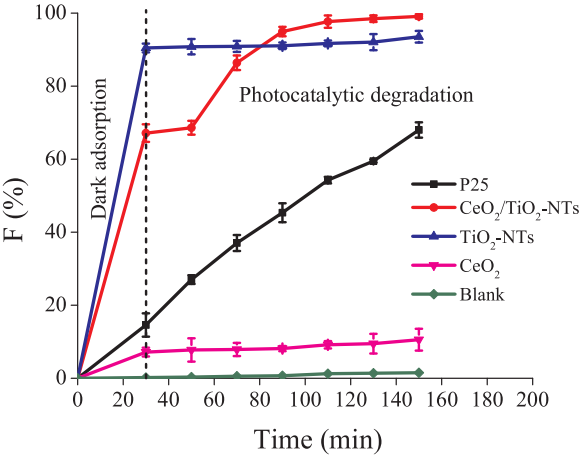

Fig. 12. Degradation efficiency of MB solution during visible light illumination over TiO_2–NTs, P25, CeO_2, CeO_2/TiO_2–NTs and blank (V = 100 mL, $C_{0(MB)}$ = 15 ppm, $m_{catalyst}$ = 0.08 g, illumination time: 120 min, room temperature).

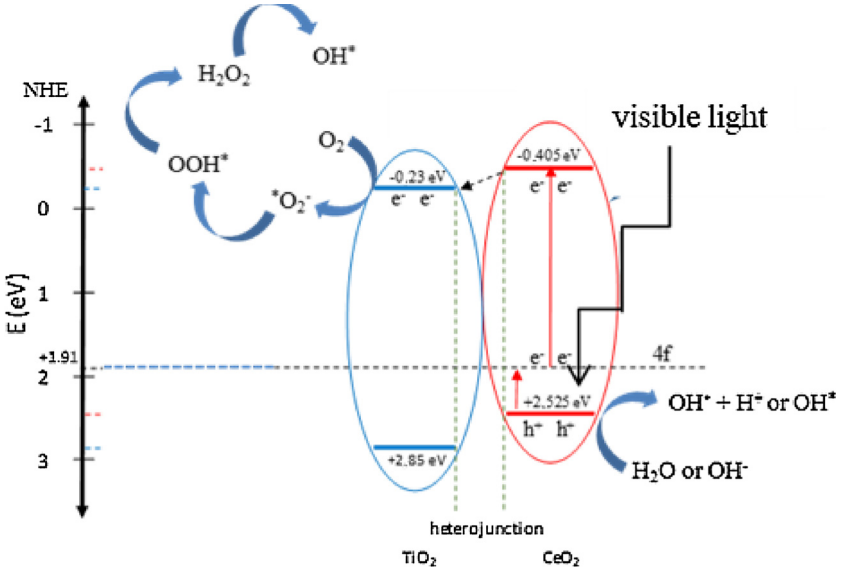

Fig. 11. Energy of valence band edge and conduction band edge for TiO_2 and CeO_2.

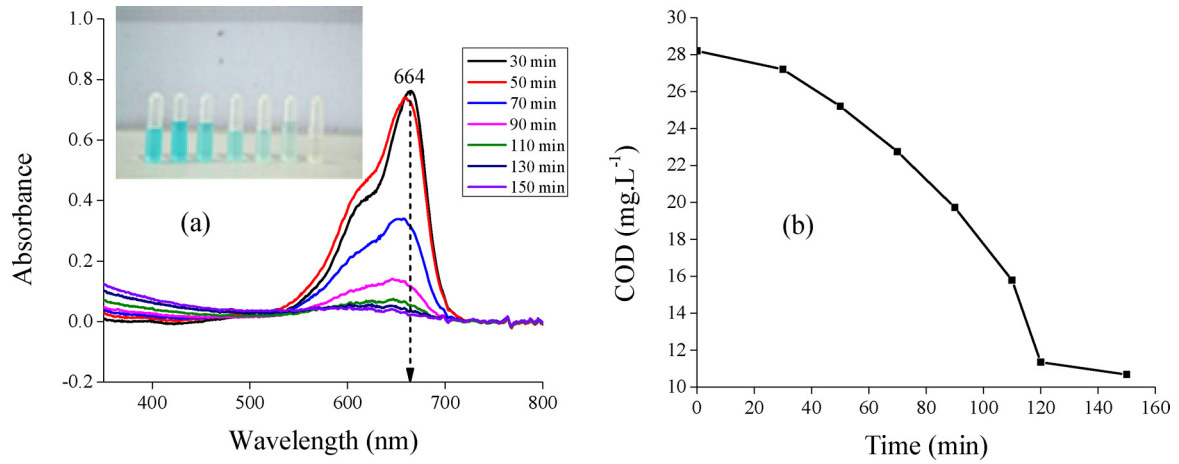

Fig. 13. Degradation of MB over CeO_2/TiO_2–NTs: a) UV–Vis spectra; b) COD value (V = 100 mL, $C_{0(MB)}$ = 15 ppm, $m_{catalyst}$ = 0.08 g, illumination time: 120 min, room temperature).

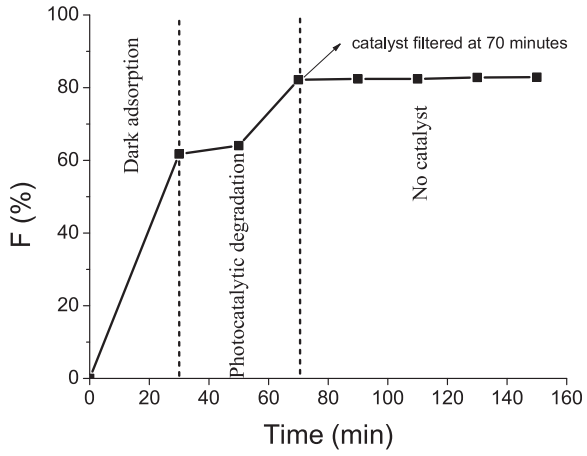

Fig. 14. Leaching experiments of CeO_2/TiO_2–NTs (V = 100 mL, $C_{0(MB)}$ = 15 ppm, $m_{catalyst}$ = 0.08 g, illumination time: 120 min, room temperature).

from 3 to 4, followed by a slow increase when the pH changed from 4 to 8 but then decreased significantly when the pH increased to 12 (Fig. 15). The point of zero charge (pH_{PZC}) of CeO_2/TiO_2–NTs estimated by the pH drift method was approximately 4 (inset of Fig. 15). At pH < 4, the MB molecule is neutral (pK_a = 3.8) [82], and the surface of the CeO_2/TiO_2–NTs was charged positively due to protonation. Therefore, the van der Waals interaction between MB and CeO_2/TiO_2–NTs could be dominant.

Such a poor interaction results in a very low efficiency of the photochemical degradation reaction. Furthermore, with the positively charged surface, the hydroxyl ion supply required for the free radical formation is limited, which is important for photocatalytic decomposition. The MB degradation increases with increasing pH because the increasing electrostatic interaction between the negatively charged surface and positive cationic dye causes a stronger photocatalytic reaction. The higher the pH is, the higher the number of hydroxyl ions at the surface of CeO_2/TiO_2–NTs will be, and hydroxyl ions give hydroxyl radicals in the following equation [46,81]:

$$h^+ + OH^- \rightarrow OH\bullet \quad (7)$$

However, the photochemical degradation is inhibited when pH is too high because the hydroxyl ion may compete with the MB molecule in the adsorption on the photocatalyst surface.

3.3.1.4. Formation of free radicals. The free radical generation by photoinduced electron-hole pairs was confirmed by the fluorescence emission spectrum. Fig. 16a shows the induction of fluorescence from 5×10^{-4} M terephthalic acid in the 2×10^{-3} M NaOH solution. The increase in the fluorescence intensity against illumination time at 425 nm was observed. The fluorescence intensity by UV light illumination in the terephthalic acid solutions increased almost linearly with time. Consequently, we can conclude that the formation of OH. at the CeO_2/TiO_2–NTs interface was proportional to the light illumination.

In order to confirm the formation of hydroxyl radicals on the catalytic interface by visible light illumination, *tert*-butanol was used as the free radical scavenger. In the presence of *tert*-butanol, a marked reduction in the MB photochemical catalytic activity was observed, and the decomposition efficiency decreased sharply when increasing the amount of tert-butanol (Fig. 16b). It can be seen from the figure that the degradation efficiency of MB decreased from 97% to 64.6% and 58.3% as 0.1 mL and 0.2 mL *tert*-butanol was added, respectively. These results confirm that the free radical mechanism plays an important role for the photocatalytic degradation.

3.3.1.5. Mechanism of photocatalytic reactions over CeO_2/TiO_2–NTs. Upon light illumination, at the hetero-junction interface of CeO_2 and TiO_2, first, CeO_2 absorbed light and the electron was excited to move from the valence band (VB) to the conduction band (CB). Then, the photoexcited electrons jumped to the conduction band of TiO_2 where the CB level (–0.405 eV) of CeO_2 is more negative than that of TiO_2 (–0.23 eV). These electrons easily reduced the surface oxygen to produce a large number of reactive oxy radicals such as superoxide radical ion $O_2^-\bullet$ and hydroxyl radicals $OOH^{\cdot}/OH^{\cdot}$ on the surface of CeO_2/TiO_2–NTs. These oxyradicals reacted with MB giving CO_2/H_2O through a number of intermediates. At the same time, the photoexcitation provided photoinduced holes at the valence band of CeO_2, which acted as a strong oxidant to oxidise H_2O or HO– [60,64], and produced the active species such as OH. (Fig. 11). Therefore, a large number of oxygenated species on the surface of the catalyst might significantly initiate the photodegradation of MB into less harmful minerals under light illumination. In addition, the deviation from ideal stoichiometry, *i.e.* CeO_{2-x} (Ce^{3+} and Ce^{4+}), leads to an occupation of the f band, which splits into an occupied part and an unoccupied part [83,84]. Therefore, the activity was found to be directly related to the presence of the Ce^{3+} species which caused the extended absorption in the visible-light region due to the populated 4f states at the interface between ceria and titania. The formation of the inter-band transition from Ce^{3+} facilitated the interfacial charge transfer, thus improving the photocatalytic degradation efficiency of the CeO_2–TiO_2 composites. Overall, the enhanced photocatalytic activity of the hybrid catalysts

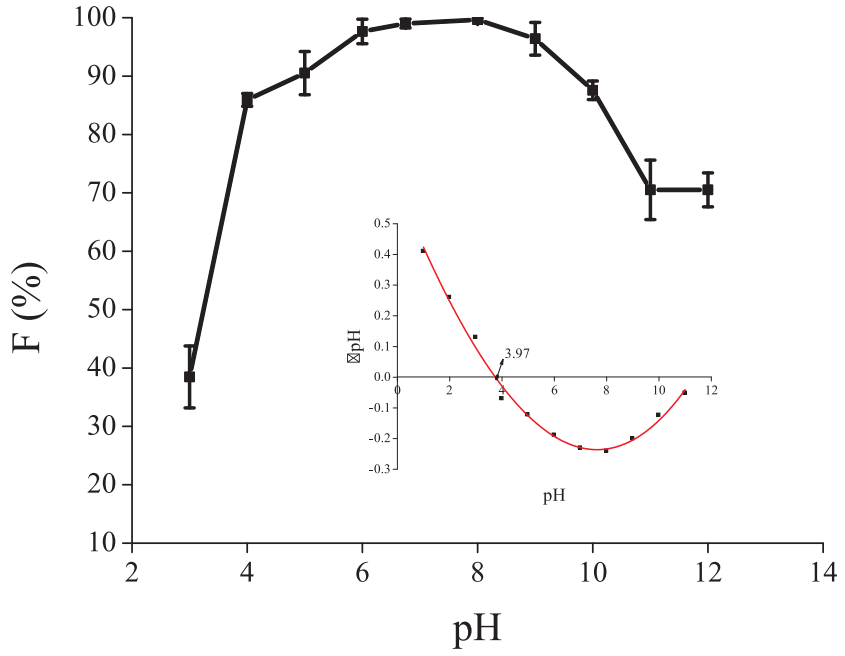

Fig. 15. Effect of pH on the degradation yield (V = 100 mL, $C_{0(MB)}$ = 15 ppm, $m_{catalyst}$ = 0.08 g, illumination time: 120 min, room temperature, pH: 3–12); the inset presents the pH_{PZC} estimated using pH drift method.

involving CeO_2 and TiO_2 could be attributed to the synergistic effects between two oxides due to the presence of hetero-junctions and the Ce^{3+} species in the composites.

The degradation reactions of MB over CeO_2/TiO_2–NTs could be illustrated as follows [65,85,86],

$$CeO_2/TiO_2 + h\lambda \rightarrow h^+ + e- \quad (8)$$

$$h^+ + H_2O \rightarrow H^+ + OH^{\cdot} \quad (9)$$

$$h^+ + OH- \rightarrow OH^{\cdot} \quad (10)$$

$$e^- + O_2 \rightarrow O_2^-\bullet \quad (11)$$

$$O_2^-\bullet + H_2O \rightarrow OOH\bullet + OH^- \quad (12)$$

$$2\ OOH^{\cdot} \rightarrow H_2O_2 + O_2 \quad (13)$$

$$H_2O_2 + e- \rightarrow OH- + OH^{\cdot} \quad (14)$$

$$Ce^{4+} + e- \rightarrow Ce^{3+} \quad (15)$$

$$Ce^{3+} + O_2 \rightarrow Ce^{4+} + O_2^-\bullet \quad (16)$$

$$(OH\bullet, O_2^-\bullet) + MB \rightarrow products \quad (17)$$

3.3.2. Photocatalytic kinetics of MB degradation over CeO_2/TiO_2–NTs

The kinetics of adsorption and photocatalytic degradation of MB on CeO_2/TiO_2–NTs are presented in Fig. 17.

The dark adsorption took place quickly and reached equilibrium at around 30 min. Afterwards, the MB concentration continued to decrease due to the reaction under visible light. It is supposed that MB was adsorbed on the catalyst and then it was decomposed on the catalyst surface under visible illumination according to the Langmuir-Hinshelwood model.

The overall reaction could be illustrated as follows

$$X + MB \underset{k_{-1}}{\overset{k_1}{\rightleftarrows}} (X...MB)^* \xrightarrow{k_2} products$$

where MB refers to methylene blue; X is the catalyst (CeO_2/TiO_2–NTs);

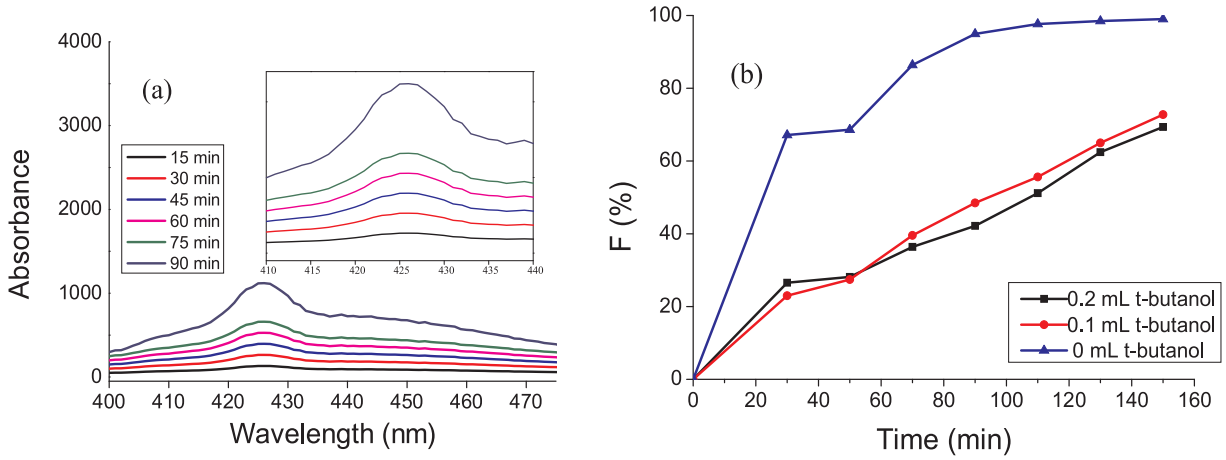

Fig. 16. a) Fluorescence spectra observed during illumination of CeO_2/TiO_2–NTs in 2×10^{-3} M NaOH solution of 5×10^{-4} M terephthalic acid. (V = 200 mL; $m_{catalyst}$ = 200 mg, illumination time: 120 min, room temperature); b. Influence of *tert*-butanol on the degradation of MB (V = 100 mL; $m_{catalyst}$ = 0.08 g, illumination time: 120 min, room temperature).

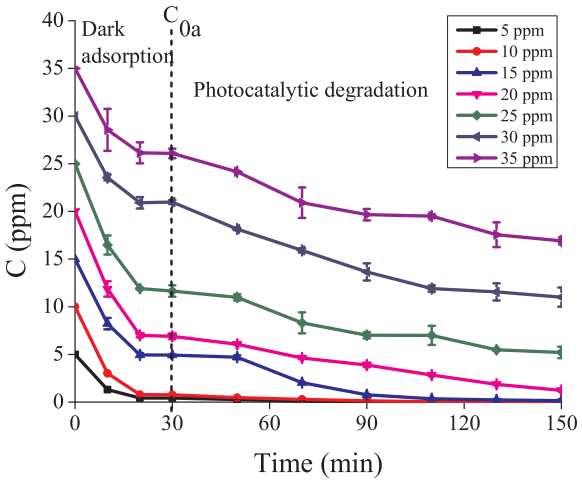

Fig. 17. Kinetics of adsorption and photocatalytic degradation of MB over CeO_2/TiO_2–NTs at different initial MB concentrations (V = 100 mL, $C_{0\,(MB)}$ = 5–35 ppm, $m_{catalyst}$ = 0.08 g, irradiation time: 120 min, room temperature).

k_1 is the forward adsorption rate constant; k_{-1} is the backward adsorption rate constant; k_2 is the photocatalytic rate constant.

Assuming that the photocatalytic degradation is the slow rate-determining step, the rate of degradation is expressed as

$$r = -\frac{dC}{dt} = k_r \cdot \theta \tag{18}$$

where θ is the fraction of the surface covered by MB.

At equilibrium, θ is expressed as follows

$$\theta = \frac{K_L \cdot C}{1 + K_L \cdot C} \tag{19}$$

Therefore,

$$r = -\frac{dC}{dt} = k_r \cdot \frac{K_L \cdot C}{1 + K_L \cdot C} \tag{20}$$

It is known that when the initial concentrations of the reactants are low, then $K_L \cdot C << 1$, and the photocatalytic reactions follow the pseudo-first-order kinetics model [87]. The kinetics Eq. (20) can be written as

$$-\frac{dC}{dt} = k_{app} \cdot C \tag{21}$$

where k_{app} (= $k_r \cdot K_L$) is the rate constant (min^{-1}).

Integrating Eq. (21) (under the boundary conditions $C = C_{0a}$ at $t = 0$; C_{0a} is the initial concentration of MB after dark adsorption, and C represents the concentration of MB at the reaction time t) provided Eq. (22)

$$\ln \frac{C_{0a}}{C} = k_{app} \cdot t \tag{22}$$

The linear plot of $\ln(C_{0a}/C)$ *vs.* t yields k_{app}. High coefficients of regression, R^2 (0.911–0.989) confirmed that the MB photocatalytic degradation fitted the L–H first-order kinetic model well. Furthermore, as shown in Table 5, the apparent first-order rate constants k_{app} declined with the increase of initial MB concentrations. This might be the result of the generated intermediate products during the photocatalytic reaction; specifically, the MB photodegradation productivity became poorer since a great number of intermediates were adsorbed on the surface of CeO_2–TiO_2–NTs, which slowed down the overall reaction rate.

Table 5
Kinetic parameters for the degradation of MB.

C_0 (ppm)	k_{app} (min^{-1})	r_0 (mg L^{-1} min^{-1})	R^2	*p-value*
5	0.036	0.18	0.989	< 0.001
10	0.034	0.34	0.979	< 0.001
15	0.032	0.48	0.970	< 0.001
20	0.014	0.28	0.967	< 0.001
25	0.007	0.15	0.911	< 0.001
30	0.005	0.15	0.958	< 0.001
35	0.004	0.13	0.956	< 0.001

The initial concentration of MB also affected its initial rate of photodegradation. As seen from Table 5, the initial photodegradation rate increased with the MB concentration up to 15 ppm from 0.18 mg L^{-1} min^{-1} to 0.48 mg L^{-1} min^{-1}; however, it decreased dramatically to 0.13 mg L^{-1} min^{-1} when the original MB concentration was 35 ppm.

The initial rate could be expressed as follows

$$K_{app} \cdot C_{0a} = k_r \cdot \frac{K_L \cdot C_{0a}}{1 + K_L \cdot C_{0a}} \tag{23}$$

Rearranging Eq. (23) gives

$$\frac{1}{k_{app}} = \frac{C_{0a}}{k_r} + \frac{1}{k_r \cdot K_L} \tag{24}$$

The plot of $1/k_{app}$ *versus* C_{0a} showed a linear variation with a high coefficient of regression (R^2 = 0.969, p = 6.10^{-5}). The values of k_r and K_L calculated from the slope and the intercept of the straight line for the photocatalytic process were 0.103 mg L^{-1} min^{-1} and 0.840 L·mg^{-1}, respectively.

3.3.3. Cycle photocatalytic degradation studies

The stability of the catalyst was evaluated by using it repeatedly. During the first two cycles, the used catalyst was separated by centrifuging, then washed with deionised water, and dried at 100 °C. The decrease of MB concentration in each cycle is represented in Fig. 18. After each cycle, a slight activity loss was observed (around 2%). This indicates that the CeO_2/TiO_2–NTs was a robust stable catalyst.

4. Conclusions

The synthesis and photocatalytic activity of CeO_2/TiO_2–NTs in the degradation of methylene blue were detailed in this study. The Box–Behnken design of the response surface methodology was employed to optimize the photocatalytic degradation of MB on the synthesised CeO_2/TiO_2–NTs. The model prediction of RSM fitted well with the experimental data with R^2 and adjusted R^2 of 89.4% and 77.0%, respectively. The optimization results showed that the maximal removal yield (93.4%) was obtained at the optimum synthesis conditions:

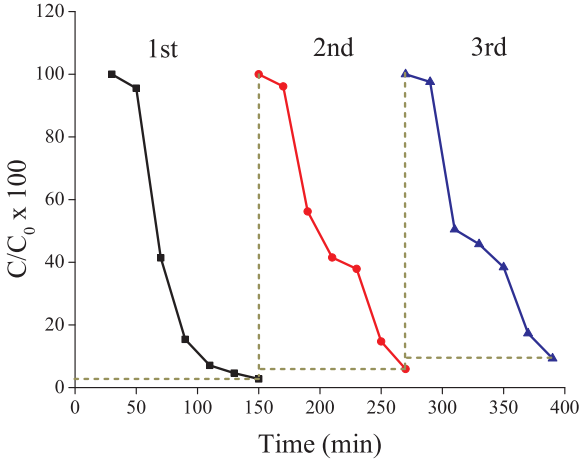

Fig. 18. Regeneration of CeO_2/TiO_2–NTs after three recycles (V = 100 mL, $C_{0\,(MB)}$ = 15 ppm, $m_{catalyst}$ = 0.08 g, illumination time: 120 min, room temperature).

hydrothermal temperature of 160 °C, calcination temperature of 550 °C, hydrothermal time of 20 h, and CeO_2/TiO_2 molar ratio of 0.1. The results clearly demonstrated that the response surface methodology (RSM) with the Box–Behnken design was one of the reliable methods for modeling and optimisation of the synthesis variables. CeO_2 as a dopant for TiO_2–NTs brought a red shift and drove the band gap to the visible light region and efficiently hindered the recombination of photoinduced electron-hole pairs. Consequently, the photocatalytic activity of CeO_2/TiO_2 increased significantly in the visible region compared with each individual oxide. The synthesised catalyst was stable after three recycles without metal leaching. These results suggested CeO_2/TiO_2–NTs to be a promising catalyst for the heterogeneous photocatalytic dye degradation in the visible region.

Acknowledgements

This research is funded by National Foundation for Science and Technology Development (NAFOSTED), Vietnam; grant IDs: 104.06-2017.311.

References

[1] H. Eskandarloo, A. Badiei, M.A. Behnajady, TiO2/CeO2 hybrid photocatalyst with enhanced photocatalytic activity: optimization of synthesis variables, Ind. Eng. Chem. Res. 53 (2014) 7847–7855.
[2] W. Xue, G. Zhang, X. Xu, X. Yang, C. Liu, Y. Xu, Preparation of titania nanotubes doped with cerium and their photocatalytic activity for glyphosate, Chem. Eng. J. 167 (2011) 397–402.
[3] M. Hussain, R. Ceccarelli, D.L. Marchisio, D. Fino, N. Russo, F. Geobaldo, Synthesis, characterization, and photocatalytic application of novel TiO2 nanoparticles, Chem. Eng. J. 157 (2010) 45–51.
[4] K. Shankar, J.I. Basham, N.K. Allam, O.K. Varghese, G.K. Mor, X. Feng, M. Paulose, J.A. Seabold, K.-S. Choi, C.A. Grimes, Recent advances in the use of TiO2 nanotube and nanowire arrays for oxidative photoelectrochemistry, J. Phys. Chem. C 113 (2009) 6327–6359.
[5] S. Pavasupree, S. Ngamsinlapasathian, Y. Suzuki, S. Yoshikawa, Synthesis and dye-sensitized solar cell performance of nanorods/nanoparticles TiO2 from high surface area nanosheet TiO2, J. Nanosci. Nanotechnol. 6 (2006) 3685–3692.
[6] F. Zhang, C. Zhang, H. Peng, H. Cong, H. Qian, Near-infrared photocatalytic up-conversion nanoparticles/TiO2 nanofibers assembled in large scale by electrospinning, Part. Part. Syst. Charact. 33 (2016) 248–253.
[7] W. Guo, F. Zhang, C. Lin, Z.L. Wang, Direct growth of TiO2 nanosheet arrays on carbon fibers for highly efficient photocatalytic degradation of methyl orange, Adv. Mater. 24 (2012) 4761–4764.
[8] B.-K. Min, S.-D. Choi, SnO2 thin film gas sensor fabricated by ion beam deposition, Sensors Actuators B Chem. 98 (2004) 239–246.
[9] Q. Tian, W. Wu, S. Yang, J. Liu, W. Yao, F. Ren, C. Jiang, Zinc oxide coating effect for the dye removal and photocatalytic mechanisms of flower-like MoS 2 nanoparticles, Nanoscale Res. Lett. 12 (2017) 221.
[10] Q. Tian, W. Yao, Z. Wu, J. Liu, L. Liu, W. Wu, C. Jiang, Full-spectrum-activated Z-scheme photocatalysts based on NaYF 4: Yb 3 + /Er 3 +, TiO 2 and Ag 6 Si 2 O 7, J. Mater. Chem. A 5 (2017) 23566–23576.
[11] D.V. Bavykin, V.N. Parmon, A.A. Lapkin, F.C. Walsh, The effect of hydrothermal conditions on the mesoporous structure of TiO2 nanotubes, J. Mater. Chem. 14 (2004) 3370.
[12] F. Song, Y. Zhao, Q. Zhong, Adsorption of carbon dioxide on amine-modified TiO2 nanotubes, J. Environ. Sci. 25 (2013) 554–560.
[13] K. Rajeshwar, M.E. Osugi, W. Chanmanee, C.R. Chenthamarakshan, M.V.B. Zanoni, P. Kajitvichyanukul, R. Krishnan-Ayer, Heterogeneous photocatalytic treatment of organic dyes in air and aqueous media, J. Photochem. Photobiol. C Photochem. Rev. 9 (2008) 171–192.
[14] M. Kim, S.-H. Hwang, S.K. Lim, S. Kim, Effects of ion exchange and calcinations on the structure and photocatalytic activity of hydrothermally prepared titanate nanotubes, Cryst. Res. Technol. 47 (2012) 1190–1194.
[15] V. Likodimos, T. Stergiopoulos, P. Falaras, J. Kunze, P. Schmuki, Phase composition, size, orientation, and antenna effects of self-assembled anodized titania nanotube arrays: a polarized micro-raman investigation, J. Phys. Chem. C 112 (2008) 12687–12696.
[16] G.K. Mor, O.K. Varghese, M. Paulose, K. Shankar, C.A. Grimes, A review on highly ordered, vertically oriented TiO2 nanotube arrays: fabrication, material properties, and solar energy applications, Sol. Energy Mater. Sol. Cells 90 (2006) 2011–2075.
[17] C.L. Wong, Y.N. Tan, A.R. Mohamed, A review on the formation of titania nanotube photocatalysts by hydrothermal treatment, J. Environ. Manage. 92 (2011) 1669–1680.
[18] T. Kasuga, M. Hiramatsu, A. Hoson, T. Sekino, K. Niihara, Titania nanotubes prepared by chemical processing, Adv. Mater. 11 (1999) 1307.
[19] J. Yu, H. Yu, Facile synthesis and characterization of novel nanocomposites of titanate nanotubes and rutile nanocrystals, Mater. Chem. Phys. 100 (2006) 507–512.
[20] X. Chen, S. Cao, X. Weng, H. Wang, Z. Wu, Effects of morphology and structure of titanate supports on the performance of ceria in selective catalytic reduction of NO, Catal. Commun. 26 (2012) 178–182.
[21] A.A. Farghali, A.H. Zaki, M.H. Khedr, B. Suef, Hydrothermally synthesized TiO2 nanotubes and nanosheets for photocatalytic degradation of color yellow sunset, Int. J. Adv. Res. 2 (2014) 285–291.
[22] L. Peng, T. Xie, Y. Lu, H. Fan, D. Wang, Synthesis, photoelectric properties and photocatalytic activity of the Fe2O3/TiO2 heterogeneous photocatalysts, Phys. Chem. Chem. Phys. 12 (2010) 8033.
[23] R. Nadarajan, W.A. Wan Abu Bakar, R. Ali, R. Ismail, Effect of structural defects towards the performance of TiO2/SnO2/WO3 photocatalyst in the degradation of 1,2-dichlorobenzene, J. Taiwan Inst. Chem. Eng. 64 (2016) 106–115.
[24] J. Wang, G. Ji, Y. Liu, M.A. Gondal, X. Chang, Cu2O/TiO2 heterostructure nanotube arrays prepared by an electrodeposition method exhibiting enhanced photocatalytic activity for CO2 reduction to methanol, Catal. Commun. 46 (2014) 17–21.
[25] Y. Wang, B. Li, C. Zhang, L. Cui, S. Kang, X. Li, L. Zhou, Ordered mesoporous CeO2-TiO2 composites: highly efficient photocatalysts for the reduction of CO2 with H2O under simulated solar irradiation, Appl. Catal. B Environ. 130–131 (2013) 277–284.
[26] M.M. Momeni, Y. Ghayeb, M. Davarzadeh, Single-step electrochemical anodization for synthesis of hierarchical WO3-TiO2 nanotube arrays on titanium foil as a good photoanode for water splitting with visible light, J. Electroanal. Chem. Lausanne (Lausanne) 739 (2015) 149–155.
[27] J. Qian, Z. Chen, C. Liu, X. Lu, F. Wang, M. Wang, Improved visible-light-driven photocatalytic activity of CeO2 microspheres obtained by using lotus flower pollen as biotemplate, Mater. Sci. Semicond. Process. 25 (2014) 27–33.
[28] T. Montini, M. Melchionna, M. Monai, P. Fornasiero, Fundamentals and catalytic applications of CeO2-based materials, Chem. Rev. 116 (2016) 5987–6041.
[29] D.A. Andersson, S.I. Simak, N.V. Skorodumova, I.A. Abrikosov, B. Johansson, Theoretical study of Ce O2 doped with tetravalent ions, Phys. Rev. B - Condens. Matter Mater. Phys. 76 (2007) 1–10.
[30] C. Sun, H. Li, L. Chen, Nanostructured ceria-based materials: synthesis, properties, and applications, Energy Environ. Sci. 5 (2012) 8475.
[31] M.R. Mohammadi, D.J. Fray, Nanostructured TiO2-CeO2 mixed oxides by an aqueous sol-gel process: effect of Ce:Ti molar ratio on physical and sensing properties, Sens. Actuators B Chem. 150 (2010) 631–640.
[32] M. Reli, N. Ambrožová, M. Šihor, L. Matějová, L. Čapek, L. Obalová, Z. Matěj, A. Kotarba, K. Kočí, Novel cerium doped titania catalysts for photocatalytic decomposition of ammonia, Appl. Catal. B Environ. 178 (2015) 108–116.
[33] Q. Huang, T. Gao, F. Niu, D. Chen, Z. Chen, L. Qin, X. Sun, Y. Huang, K. Shu, Preparation and enhanced visible-light driven photocatalytic properties of Au-loaded TiO2 nanotube arrays, Superlattices Microstruct. 75 (2014) 890–900.
[34] C. Fan, P. Xue, Y. Sun, Preparation of Nano-TiO2 doped with cerium and its photocatalytic activity, J. Rare Earths 24 (2006) 309–313.
[35] T. Lundstedt, E. Seifert, L. Abramo, B. Thelin, Å. Nyström, J. Pettersen, R. Bergman, Experimental design and optimization, Chemometr. Intell. Lab. Syst. 42 (1998) 3–40.
[36] N.A. Eleburuike, W.A. Wan Abu Bakar, R. Ali, M.F. Omar, Photocatalytic degradation of paraquat dichloride over CeO 2 -modified TiO 2 nanotubes and the optimization of parameters by response surface methodology, RSC Adv. 6 (2016) 104082–104093.
[37] C.-C. Tsai, H. Teng, Regulation of the physical characteristics of titania nanotube aggregates synthesized from hydrothermal treatment, Chem. Mater. 16 (2004) 4352–4358.
[38] N. Viriya-empikul, T. Charinpanitkul, N. Sano, A. Soottitantawat, T. Kikuchi, K. Faungnawakij, W. Tanthapanichakoon, Effect of preparation variables on morphology and anatase–brookite phase transition in sonication assisted hydrothermal reaction for synthesis of titanate nanostructures, Mater. Chem. Phys. 118 (2009) 254–258.
[39] N. Liu, X. Chen, J. Zhang, J.W. Schwank, A review on TiO2-based nanotubes synthesized via hydrothermal method: formation mechanism, structure modification, and photocatalytic applications, Catal. Today 225 (2014) 34–51.
[40] H. Zhao, Y. Dong, P. Jiang, G. Wang, J. Zhang, Highly dispersed CeO 2 on TiO 2 nanotube: a synergistic nanocomposite with superior peroxidase-like activity, ACS Appl. Mater. Interfaces 7 (2015) 6451–6461.
[41] S.L.C. Ferreira, R.E. Bruns, H.S. Ferreira, G.D. Matos, J.M. David, G.C. Brandão, E.G.P. da Silva, L.A. Portugal, P.S. dos Reis, A.S. Souza, W.N.L. dos Santos, Box-Behnken design: an alternative for the optimization of analytical methods, Anal. Chim. Acta 597 (2007) 179–186.
[42] S.L.C. Ferreira, R.E. Bruns, E.G.P. da Silva, W.N.L. dos Santos, C.M. Quintella, J.M. David, J.B. de Andrade, M.C. Breitkreitz, I.C.S.F. Jardim, B.B. Neto, Statistical designs and response surface techniques for the optimization of chromatographic systems, J. Chromatogr. A 1158 (2007) 2–14.
[43] M.A. Bezerra, R.E. Santelli, E.P. Oliveira, L.S. Villar, L.A. Escaleira, Response surface methodology (RSM) as a tool for optimization in analytical chemistry, Talanta 76 (2008) 965–977.
[44] J. Zolgharnein, A. Shahmoradi, J.B. Ghasemi, Comparative study of Box-Behnken, central composite, and Doehlert matrix for multivariate optimization of Pb (II) adsorption onto Robinia tree leaves, J. Chemom. 27 (2013) 12–20.
[45] A. Niazi, N. Khorshidi, P. Ghaemmaghami, Microwave-assisted of dispersive liquid-liquid microextraction and spectrophotometric determination of uranium after optimization based on Box-Behnken design and chemometrics methods, Spectrochim. Acta - Part A Mol. Biomol. Spectrosc. 135 (2015) 69–75.
[46] Y. Chen, Z. Sun, Y. Yang, Q. Ke, Heterogeneous photocatalytic oxidation of polyvinyl alcohol in water, J. Photochem. Photobiol. A: Chem. 142 (2001) 85–89.
[47] W. Jiang, J.A. Joens, D.D. Dionysiou, K.E. O'Shea, Optimization of photocatalytic performance of TiO2 coated glass microspheres using response surface methodology and the application for degradation of dimethyl phthalate, J. Photochem.

Photobiol. A: Chem. 262 (2013) 7–13.
[48] Arnold E. Greenberg, R.Rhodes Trussell, Lenore S. Clesceri, Mary Ann H. Franson, Water Pollution Control Federation; Standard methods for the examination of water and wastewater, American Public Health Association, Washington, D.C, 2018 16th Edition. c1985, American Water Works Association.
[49] E. Haque, V. Lo, A.I. Minett, A.T. Harris, T.L. Church, Dichotomous adsorption behaviour of dyes on an amino-functionalised metal–organic framework, amino-MIL-101(Al), J. Mater. Chem. A 2 (2014) 193–203.
[50] B.H. Dang Son, V. Quang Mai, D. Xuan Du, N. Hai Phong, D. Quang Khieu, A study on astrazon black AFDL dye adsorption onto Vietnamese diatomite, J. Chem. 2016 (2016).
[51] P. Burroughs, A. Hamnett, A.F. Orchard, G. Thornton, Satellite structure in the X-ray photoelectron spectra of some binary and mixed oxides of lanthanum and cerium, J. Chem. Soc. Dalt. Trans. (1976) 1686.
[52] V. Fernandes, P. Schio, A.J.A. de Oliveira, W.A. Ortiz, P. Fichtner, L. Amaral, I.L. Graff, J. Varalda, N. Mattoso, W.H. Schreiner, D.H. Mosca, Ferromagnetism induced by oxygen and cerium vacancies above the percolation limit in CeO_2, J. Phys. Condens. Matter 22 (2010) 216004.
[53] C. Gionco, M.C. Paganini, S. Agnoli, A.E. Reeder, E. Giamello, Structural and spectroscopic characterization of CeO2–TiO2 mixed oxides, J. Mater. Chem. A 1 (2013) 10918.
[54] B. Choudhury, P. Chetri, A. Choudhury, Oxygen defects and formation of Ce^{3+} affecting the photocatalytic performance of CeO_2 nanoparticles, RSC Adv. 4 (2014) 4663–4671.
[55] W. Zhu, S. Xiao, D. Zhang, P. Liu, H. Zhou, W. Dai, F. Liu, H. Li, Highly efficient and stable Au/CeO 2 –TiO 2 photocatalyst for nitric oxide abatement: potential application in flue gas treatment, Langmuir 31 (2015) 10822–10830.
[56] Y. Wang, J. Zhao, T. Wang, Y. Li, X. Li, J. Yin, C. Wang, CO2 photoreduction with H2O vapor on highly dispersed CeO2/TiO2 catalysts: surface species and their reactivity, J. Catal. 337 (2016) 293–302.
[57] F.W. Clarke, B. Irving Langmuir, Constitution of solids and liquids, J. Am. Chem. Soc. 38 (1916) 2221–2295.
[58] T.M.F. Marques, O.P. Ferreira, J.A.P. Da Costa, K. Fujisawa, M. Terrones, B.C. Viana, Study of the growth of CeO22 nanoparticles onto titanate nanotubes, J. Phys. Chem. Solids 87 (2015) 213–220.
[59] J. Jiao, Y. Wei, Z. Zhao, J. Liu, J. Li, A. Duan, G. Jiang, Photocatalysts of 3D ordered macroporous TiO 2 -supported CeO 2 nanolayers: design, preparation, and their catalytic performances for the reduction of CO 2 with H 2 O under simulated solar irradiation, Ind. Eng. Chem. Res. 53 (2014) 17345–17354.
[60] D. Tomova, V. Iliev, A. Eliyas, S. Rakovsky, Promoting the oxidative removal rate of oxalic acid on gold-doped CeO2/TiO2 photocatalysts under UV and visible light irradiation, Sep. Purif. Technol. 156 (2015) 715–723.
[61] J. Graciani, J.J. Plata, J.F. Sanz, P. Liu, J.A. Rodriguez, A theoretical insight into the catalytic effect of a mixed-metal oxide at the nanometer level: the case of the highly active metal/CeOx/TiO2(110) catalysts, J. Chem. Phys. 132 (2010) 104703.
[62] V.V. Atuchin, V.G. Kesler, N.V. Pervukhina, Z. Zhang, Ti 2p and O 1s core levels and chemical bonding in titanium-bearing oxides, J. Electron Spectros. Relat. Phenomena 152 (2006) 18–24.
[63] Z. Zhang, Z. Zhou, S. Nie, H. Wang, H. Peng, G. Li, K. Chen, Flower-like hydrogenated TiO2(B) nanostructures as anode materials for high-performance lithium ion batteries, J. Power Sources 267 (2014) 388–393.
[64] X. Lu, X. Li, J. Qian, N. Miao, C. Yao, Z. Chen, Synthesis and Characterization of CeO 2 / TiO 2 Nanotube Arrays and Enhanced Photocatalytic Oxidative Desulfurization Performance 661 (2016), pp. 363–371.
[65] C. Hao, J. Li, Z. Zhang, Y. Ji, H. Zhan, F. Xiao, D. Wang, B. Liu, F. Su, Enhancement of photocatalytic properties of TiO2 nanoparticles doped with CeO2 and supported on SiO2 for phenol degradation, Appl. Surf. Sci. 331 (2015) 17–26.
[66] C. Karunakaran, P. Gomathisankar, Solvothermal synthesis of CeO 2 –TiO 2 nanocomposite for visible light photocatalytic detoxification of cyanide, ACS Sustain. Chem. Eng. 1 (2013) 1555–1563.
[67] Z. Shi, P. Yang, F. Tao, R. Zhou, New insight into the structure of CeO 2 –TiO 2 mixed oxides and their excellent catalytic performances for 1,2-dichloroethane oxidation, Chem. Eng. J. 295 (2016) 99–108.
[68] B. Yuan, Y. Long, L. Wu, K. Liang, H. Wen, S. Luo, H. Huo, H. Yang, J. Ma, TiO2@ h-CeO2: a composite yolk-shell microsphere with enhanced photodegradation activity, Catal. Sci. Technol. 6 (2016) 6396–6405.
[69] C. Ampelli, R. Passalacqua, C. Genovese, S. Perathoner, G. Centi, T. Montini, V. Gombac, P. Fornasiero, Solar energy and biowaste conversion into H2 on CuO x/TiO2 nanocomposites, Chem. Eng. Trans. 35 (2013) 583–588.
[70] L. Matějová, K. Kočí, M. Reli, L. Čapek, A. Hospodková, P. Peikertová, Z. Matěj, L. Obalová, A. Wach, P. Kuśtrowski, A. Kotarba, Preparation, characterization and photocatalytic properties of cerium doped TiO2: on the effect of Ce loading on the photocatalytic reduction of carbon dioxide, Appl. Catal. B Environ. 152–153 (2014) 172–183.
[71] X. Yang, L. Yang, J. Lin, R. Zhou, The new insight into the structure-activity relation of Pd/CeO_2 -ZrO_2 -Nd_2O_3 catalysts by Raman, in situ DRIFTS and XRD Rietveld analysis, Phys. Chem. Chem. Phys. 18 (2015) 3103–3111.
[72] A.I. Kontos, A.G. Kontos, D.S. Tsoukleris, G.D. Vlachos, P. Falaras, Superhydrophilicity and photocatalytic property of nanocrystalline titania sol–gel films, Thin Solid Films 515 (2007) 7370–7375.
[73] M. Guo, J. Lu, Y. Wu, Y. Wang, M. Luo, UV and visible Raman studies of oxygen vacancies in rare-earth-doped ceria, Langmuir 27 (2011) 3872–3877.
[74] A. Filtschew, K. Hofmann, C. Hess, Ceria and its defect structure: new insights from a combined spectroscopic approach, J. Phys. Chem. C 120 (2016) 6694–6703.
[75] T.M.F. Marques, O.P. Ferreira, J.A.P. da Costa, K. Fujisawa, M. Terrones, B.C. Viana, Study of the growth of CeO2 nanoparticles onto titanate nanotubes, J. Phys. Chem. Solids 87 (2015) 213–220.
[76] M.E. Contreras-Garc??a, M.L. Garc??a-Benjume, V.I. Mac??as-Andr??s, E. Barajas-Ledesma, A. Medina-Flores, M.I. Espitia-Cabrera, Synergic effect of the TiO2-CeO2 nanoconjugate system on the band-gap for visible light photocatalysis, Mater. Sci. Eng. B Solid-State Mater. Adv. Technol. 183 (2014) 78–85.
[77] S. Luo, T.D. Nguyen-Phan, A.C. Johnston-Peck, L. Barrio, S. Sallis, D.A. Arena, S. Kundu, W. Xu, L.F.J. Piper, E.A. Stach, D.E. Polyansky, E. Fujita, J.A. Rodriguez, S.D. Senanayake, Hierarchical heterogeneity at the CeOx-TiO2 interface: electronic and geometric structural influence on the photocatalytic activity of oxide on oxide nanostructures, J. Phys. Chem. C 119 (2015) 2669–2679.
[78] Y. Xu, M.A.A. Schoonen, The absolute energy positions of conduction and valence bands of selected semiconducting minerals, Am. Mineral. 85 (2000) 543–556.
[79] J. Tian, Y. Sang, Z. Zhao, W. Zhou, D. Wang, X. Kang, H. Liu, J. Wang, S. Chen, H. Cai, H. Huang, Enhanced photocatalytic performances of CeO2/TiO2 nanobelt heterostructures, Small 9 (2013) 3864–3872.
[80] B.H.D. Son, V.Q. Mai, D.X. Du, N.H. Phong, N.D. Cuong, D.Q. Khieu, Catalytic wet peroxide oxidation of phenol solution over Fe–Mn binary oxides diatomite composite, J. Porous Mater. 24 (2017) 601–611.
[81] J. Saien, S. Khezrianjoo, Degradation of the fungicide carbendazim in aqueous solutions with UV/TiO2 process: optimization, kinetics and toxicity studies, J. Hazard. Mater. 157 (2008) 269–276.
[82] J.R. Kim, B. Santiano, H. Kim, E. Kan, Heterogeneous oxidation of methylene blue with surface-modified iron-amended activated carbon, Am. J. Anal. Chem. 2013 (2013) 115–122.
[83] M.A. Henderson, C.L. Perkins, M.H. Engelhard, S. Thevuthasan, C.H.F. Peden, Redox properties of water on the oxidized and reduced surfaces of CeO2(1 1 1), Surf. Sci. 526 (2003) 1–18.
[84] D.R. Mullins, P.M. Albrecht, T.-L. Chen, F.C. Calaza, M.D. Biegalski, H.M. Christen, S.H. Overbury, Water dissociation on CeO 2 (100) and CeO 2 (111) thin films, J. Phys. Chem. C 116 (2012) 19419–19428.
[85] T.K. Jana, A. Pal, K. Chatterjee, Self assembled flower like CdS-ZnO nanocomposite and its photo catalytic activity, J. Alloys. Compd. 583 (2014) 510–515.
[86] a Houas, Photocatalytic degradation pathway of methylene blue in water, Appl. Catal. B Environ. 31 (2001) 145–157.
[87] K. Mehrotra, G.S. Yablonsky, A.K. Ray, Macro kinetic studies for photocatalytic degradation of benzoic acid in immobilized systems, Chemosphere 60 (2005) 1427–1436.